Publications of the Astronomical Society of the Pacific, 134:035004 (10pp), 2022 March https://doi.org/10.1088/1538-3873/ac584a
© 2022. The Astronomical Society of the Pacific. All rights reserved.

Astrometric Precision Tests on TESS Data

M. Gai[1], A. Vecchiato[1], A. Riva[1], D. Busonero[1], M. Lattanzi[1], B. Bucciarelli[1], M. Crosta[1], and Z. Qi[2]
[1] Ist. Naz. di Astrofisica—Osserv. Astrofisico di Torino, V. Osservatorio, 20, I-10025 Pino Torinese (TO), Italy
[2] Shanghai Astron. Observatory, Chinese Academy of Sciences, 80 Nandan Rd, Shanghai 200030, People's Republic of China
Received 2021 November 25; accepted 2022 February 24; published 2022 April 4

Abstract

Astrometry at or below the microarcsec level with an imaging telescope assumes that the uncertainty on the location of an unresolved source can be an arbitrarily small fraction of the detector pixel, given a sufficient photon budget. This paper investigates the geometric limiting precision, in terms of CCD pixel fraction, achieved by a large set of star field images, selected among the publicly available science data of the Transiting Exoplanet Survey Satellite (TESS) mission. The statistics of the distance between selected bright stars ($G \simeq 5$ mag), in pixel units, is evaluated, using the position estimate provided in the TESS light curve files. The dispersion of coordinate differences appears to be affected by long term variation and noisy periods, at the level of 0.01 pixel. The residuals with respect to low-pass filtered data (tracing the secular evolution), which are interpreted as the experimental astrometric noise, reach the level of a few milli-pixel or below, down to 1/5900 pixel. Saturated images are present, evidencing that the astrometric precision is mostly preserved across the CCD columns, whereas it features a graceful degradation in the along column direction. The cumulative performance of the image set is a few micropixel across columns, or a few 10 μpx along columns. The idea of astrometric precision down to a small fraction of a CCD pixel, given sufficient signal to noise ratio, is confirmed by real data from an in-flight science instrument to the 10^{-6} pixel level. Implications for future high precision astrometry missions are briefly discussed.

Unified Astronomy Thesaurus concepts: Astronomical detectors (84); Space astrometry (1541); Optical observation (1169); Space telescopes (1547)

1. Introduction

One of the basic tasks of astrometry is to find, in an image, the position of one photon distribution, generated by an object, with respect to the pixel array, and/or other similar signals. The matter is discussed in several contexts in the literature (Lindegren 1978; Gai et al. 1998; Mendez et al. 2014), and it has also been addressed in a direct experimental way (Gai et al. 2001, 2020a).

Future missions for Astrophysics and Fundamental Physics, e.g., Theia (Malbet et al. 2021), AGP (Gai et al. 2020b), TOLIMAN (Tuthill et al. 2018; Bendek et al. 2021), aim at significant improvements on astrometric precision for limited samples of objects (few tens to few hundreds, reaching the regime 0.1–1 μas. This, on 1 m class telescopes with focal length ~30 m, results in a tiny fraction of the pixel size, which with current CCD technology is of order of 10 μm or not much smaller; CMOS devices are getting close to adequate scientific performance (Gil Otero et al. 2021), and have slightly smaller pixels (e.g., ~2 μm), also claiming better radiation tolerance. Since the angular pixel size is a few ten milli-arcsec (mas), the goal precision of the measurements translates in a relative value of 10^{-5}–10^{-6}.

Among the challenges identified to actually reach such precision level, we may focus on at least three issues potentially introducing significant systematic errors:

1. the field variation of telescope optical response;
2. the variation of electro-optical response over the detector;
3. a "Cosmic noise," i.e., the variability of individual astronomical objects.

The authors are engaged in a collaboration (Gai et al. 2020a) aimed at studying selected topics in such areas; early results e.g., on the first topic have been reported in the literature (Riva et al. 2020). We remark that the former two aspects are mostly focused on technological aspects, whereas the latter also depends on the selected targets. The measurement approaches proposed for implementation of specific science cases may shift the weight among the areas, leading e.g., to different development requirements.

A celestial source, even when unresolved, i.e., its angular size is negligible with respect to the resolving power of a given imaging instrument, still has a minimum uncertainty related to the size of the Point-Spread Function (PSF), imposed by diffraction. The estimated position of a reference point of the distribution, hereafter the photocenter, is affected by an uncertainty which also depends on the signal level: since measured values are affected by fluctuations (shot noise), the parent distribution is traced more faithfully by a larger number N of photons, involving lower relative variation ($\sim 1/\sqrt{N}$). As a result, the location uncertainty for an unresolved source is

roughly proportional to the image diffraction size divided by the photometric signal to noise ratio (S/N), with corrections at the faint end for the degradation due e.g., to background and readout noise, and at the bright end because of saturation and/or nonlinearity. In the bright regime, we may usually approximate the location uncertainty σ as

$$\sigma \simeq \alpha \frac{\lambda_{\rm eff}}{D \cdot {\rm S/N}}, \quad (1)$$

where $\lambda_{\rm eff}$ is the effective wavelength of observation, D the telescope diameter, and α a scaling parameter summarizing contributions from the instrument geometry and optical quality (hence diffraction image size), operations and algorithm (Gai et al. 2017). The general trend of precision with source magnitude is extensively verified on the $>10^9$ objects observed by the mission Gaia (Prusti et al. 2016; Gaia Collaboration et al. 2020), which in the bright part of the sample achieves few tens of microarcsec (μas) on positions and parallaxes, and few μas yr^{-1} on proper motions (further improvements expected on the final data release in 2028).

The (one-dimensional) distance between sources 1, 2 is then dominated by the uncertainty on the fainter one, associated to lower S/N:

$$\sigma_{1,2} \simeq \alpha \frac{\lambda_{\rm eff}}{D} \sqrt{\left(\frac{1}{{\rm S/N_1}}\right)^2 + \left(\frac{1}{{\rm S/N_2}}\right)^2}. \quad (2)$$

Astrometric measurements are often implemented as a set of many observations, e.g., to derive parallax and proper motion by the position evolution through time. Also a single-epoch observation, providing an elementary position information, may be split in a sequence of elementary snapshots for a number of practical reasons. Apart other considerations, in order to achieve the above mentioned precision on location, in a system with diffraction image size comparable with one pixel, it is necessary to achieve an extremely high overall S/N (in the 10^5–10^6 range), according to Equation (1), which may be achieved by composition of many elementary exposures.

The rationale for testing the conceptual framework of astrometric precision improvement with decreasing magnitude, or increasing S/N, is that we may expect deviations from the relationship summarized by Equation (1) as soon as the predicted error becomes small enough to be comparable with other sources of noise, and/or systematic errors. They may be induced e.g., by variation of the telescope optical response, or by peculiarity in the detector response (nonlinearity, saturation, ...).

Observations are expected to have pointing errors, inducing wobbling and drift of the detected star positions; however, pointing is supposed to act mainly as a common mode displacement, without perturbing the separation between targets. Higher order effects may still be induced, e.g., by distortion.

The test we propose consists in evaluating the statistics of the separation of images of unresolved sources (hereafter, stars) over a set of frames. The consistency of the location noise with purely random noise may provide useful indications, both from a qualitative and quantitative standpoint: the former on systematic effects, and the latter on additional contributions to the photon noise.

We find a convenient source of experimental data in the publicly available science database of the Transiting Exoplanet Survey Satellite (TESS) space mission, briefly described in Section 2 with its main products, even if the mission was not designed for astrometry. Our analysis of selected data sets is detailed in Section 2.1, evidencing a number of findings of interest with respect to our goal. Some of the peculiar aspects of the results, their possible origin, and the implications for future high precision astrometry missions are discussed in Section 4. Finally, we outline our current understanding of the matter, and possible further developments, in Section 5.

2. TESS Science Data and Analysis Methods

The TESS (Ricker et al. 2015; Guerrero et al. 2021), launched in 2018, is a NASA mission led by MIT and aimed at detection of transiting exoplanets around the nearest, brightest stars. Throughout its two-year Prime Mission, TESS observed about 70% of the sky, split in 26 observing sectors, with observing times ranging from ∼1 month near the ecliptic to ∼1 yr near the ecliptic poles. Observation is focused on a list of stars, the TESS Input Catalog (TIC), described in the literature (Stassun et al. 2018, 2019).

TESS inherits many concepts from NASA's Kepler mission (Borucki et al. 2010; Howell et al. 2014), with the goal of detection and characterization of small planets. The TESS payload includes four cameras with field of view of $24^\circ \times 24^\circ$, observing a $24^\circ \times 96^\circ$ sky strip (a sector) along the selected ecliptic longitude for two orbits (∼27 days). Each camera's detector is a 2×2 mosaic of back-illuminated MIT/Lincoln Laboratory CCID-80 frame transfer devices, with $2k \times 2k$ imaging area. The angular size of the square pixel is $21''$ (15 μm linear).

The transit method implies target observation over extended time intervals, in order to detect the photometric variations during the partial eclipses of the parent star by the minor body. Elementary 2 s images are digitally stacked in sets of 60 frames, providing an effective 120 s elementary exposure; sub-arrays around the pre-selected targets ("postage stamps") are stored for download. The sub-array size depends on the individual target magnitude, with the photoelectrons from bright, saturated stars spreading over many pixels around the optical PSF. Such sets of sub-arrays, collected over a ∼27 days period (∼19,000 instances), implement the condition of repeated measurement of a stellar field suited to our statistical tests.

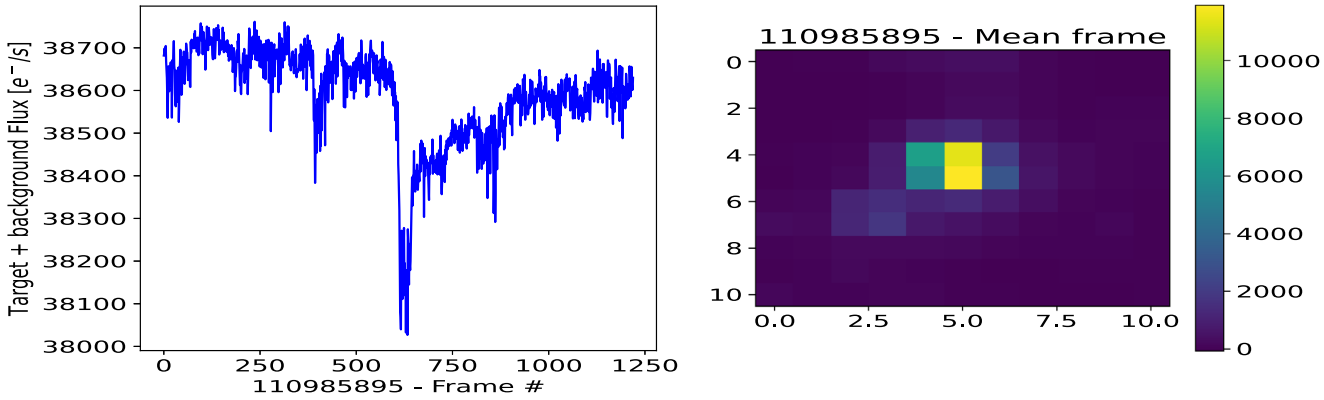

Figure 1. Light curve (left) and mean frame for one TESS observation of TIC 110985895.

The TESS data processing pipeline produces calibrated data in the form of time series of flux values (light curves), in $e^-\,s^{-1}$, and also records a copy of the calibrated sub-arrays (target pixel files). Such data are in the public domain, and available at the Barbara A. Mikulski Archive for Space Telescopes (MAST) Portal (https://mast.stsci.edu/), hosted at the Space Telescope Science Institute (STScI), which allows download of light curve, target pixel, and data validation files for selected targets.

Hereafter, targets are addressed by their TIC ID, which also identifies them in the SIMBAD Astronomical Database (CDS, Strasbourg). For example, TIC 110985895 is HD 338425, a $G = 9.47$ mag K0 star, observed in TESS sector 14 (start time: 2019 July 18th, 21:21:27). The light curve (left) and the mean value of the observed "postage stamps" (right) for this target are shown in Figure 1.

2.1. Source Sample

The TESS light curve files are produced by aperture photometry, and they also provide a number of auxiliary data and derived parameters (e.g., errors), including estimates of the target positions both by barycenter or Center Of Gravity (COF, labeled method of the moments in the TESS pipeline) and by PSF fitting.

We use such target position estimates to perform our proposed astrometry test, selecting pairs of bright targets observed simultaneously, mostly by the same camera and CCD. Since satellite attitude can be expected to be a significant disturbance to astrometric measurements, and instrument parameters may evolve on unknown timescales, the simultaneity condition appears to provide the best framework to minimize uncontrolled disturbances.

Our goal will be met by finding a few cases of measurements evidencing the desired statistics, i.e., low dispersion in photocenter separation determinations. More than one such case is needed to mitigate the risk that a peculiar, atypical data set was selected; however, since data are obtained manually through the above mentioned interactive interface, and development of a fully automated processing pipeline is out of the scope of our investigation, a limited number of source pairs is considered. Therefore, for practical reasons, not all sectors, cameras and CCDs of TESS are covered by our small sample.

A few source pairs are randomly picked among the large available set of TESS observations, mostly in the magnitude range $4.5 \leqslant G \leqslant 5.5$ mag.[3] In practice, candidate pairs are selected by randomly generating a list of integer numbers, interpreted as position indexes of a query of Gaia EDR3 sources (Gaia Collaboration et al. 2020). The selected Gaia sources sources, afterwards, were checked against the TESS target lists (https://tess.mit.edu/observations/target-lists/) to discard e.g., pairs located across sector boundaries. Finally, the availability of simultaneous observations is verified on MAST. In the processing, some pairs were discarded because the data quality appeared to be poor, likely due to disturbances.

The full list of our targets is reported in Table 1, including the TIC ID, the conventional star name, its G magnitude, approximate equatorial coordinates, the date of the selected observation (two observations are considered for the target pair {451860101, 450844221}), the TESS sector, and the camera and CCD involved. This allows unequivocal data retrieval from MAST. Observation of each source pair is simultaneous, and usually performed by the same camera and CCD, except for the pair {260366549, 297820335} (CCDs 2 and 1, respectively). This last case implies the potential for additional astrometric errors induced by microscopic modifications of the overall focal plane geometry (e.g., inter-CCD spacing), whereas the common CCD assumption factors out some such troubles (Lindegren et al. 2021). This was included on purpose to test if the above requirements on the selection of star pairs could be relaxed.

[3] From Gaia counts, 2636 sources are available, widely spread on the sky; ~63,000 pairs are within 15° separation.

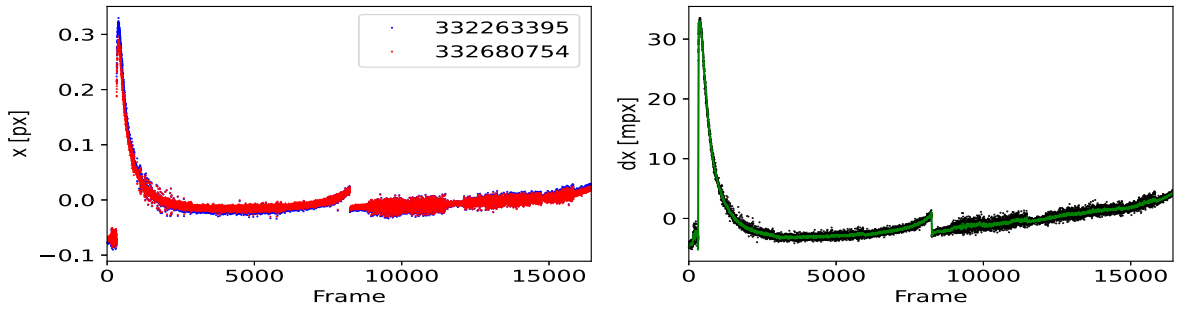

Figure 2. COG estimates on *X*-axis (left) and difference (right) for target pair {TIC 332263395, TIC 332680754}. Mean values are subtracted, and the filtered data (green line) are superposed to the COG difference.

Table 1
Targets Analysed: TIC, Common Name, *G* Magnitude, Approximate Position, Observation Details (Date, Sector, and Instrument: Camera, CCD)

TIC	Name	*G* (mag)	R.A. (deg)	Decl. (deg)	Date	Sector, Camera, CCD
332263395	HD 7733	4.7759	19.558	57.803	2019-11-03	18, 2, 2
332680754	*phi Cas	4.6769	20.020	58.232	2019-11-03	18, 2, 2
94196291	*D Vel	5.0757	130.918	−49.823	2021-03-07	36, 3, 2
30906332	V*FZ Vel	5.0842	134.718	−47.235	2021-03-07	36, 3, 2
282326777	*eta Aps	4.8056	214.558	−81.008	2021-05-27	39, 3, 2
421217840	*eps Aps	4.9494	215.597	−80.109	2021-05-27	39, 3, 2
451860101	*omi01 Cen	4.6533	172.942	−59.442	2019-03-26	10, 3, 1
450844221	V*V537 Car	4.7100	169.682	−58.186	2019-03-26	10, 3, 1
451860101	*omi01 Cen	4.6533	172.942	−59.442	2019-04-23	11, 3, 2
450844221	V*V537 Car	4.7100	169.682	−58.186	2019-04-23	11, 3, 2
60986648	*lam Ari	7.1730	29.482	23.596	2019-10-08	17, 1, 4
306342251	*kap Ari	4.9780	31.641	22.648	2019-10-08	17, 1, 4
393799555	*14 Com	4.8049	186.600	27.268	2020-02-19	22, 1, 1
393800464	*16 Com	4.8945	186.747	26.826	2020-02-19	22, 1, 1
260366549	V*SS Cep	6.1518	57.375	80.322	2019-11-28	19, 3, 2
297820335	HD 18438	4.6776	46.533	79.419	2019-11-28	19, 3, 1

The analysis is implemented in Python, using the Lightkurve package (Lightkurve Collaboration et al. 2018) for Kepler and TESS file readout, and astropy (Astropy Collaboration et al. 2013, 2018), numpy (Harris et al. 2020), Matplotlib (Hunter 2007) and other packages for data analysis.

2.2. Data Analysis Approach

An example of our assessment is shown in Figure 2, in which the light curve files for targets 332263395 and 332680754 (observed in sector 18 by camera 2, CCD 2, on 2019 November 3) have been downloaded, the estimated COG coordinate along the *X*-axis (across CCD columns) is extracted and shown in the left panel, after subtraction of the mean value, and the difference of the values, is shown in the right panel.

The X COG estimates (left panel, blue and red dots) evidence common mode jumps (approximately around frame no. 1000 and 8000) and smooth variations in time, which may be attributed to telescope pointing errors, including jitter, drift and occasional sudden transitions. The largest jump is by about 0.3 pixels (*X*) or 0.5 pixels (*Y*), whereas throughout most of the observation the fluctuations are in the order of $1/100$ pixel. Besides, as may be expected, pointing errors are mostly common mode, and the COG coordinate difference, shown in the right panel, is actually much less variable, in the few milli-pixel (hereafter, mpx) range, apart the highly disturbed period close to frame no. 1000. In practice, fluctuations on the source separation are reduced by about one order of magnitude with respect to individual coordinates.

The COG difference may be considered as an independent estimate of the source separation along the *X*-axis, and it evidences a long term behavior quite different from white noise around a constant value. The systematic variation may be due to actual changes in the instrument parameters, but also, partially, to artefacts generated within the data reduction and calibration pipeline, which was designed for photometric, rather than astrometric, purposes.

Jumps and noisy (or quiet) segments are matched on both *X* and *Y* coordinates, suggesting that they are actually related to global events affecting the satellite and/or the payload. Since

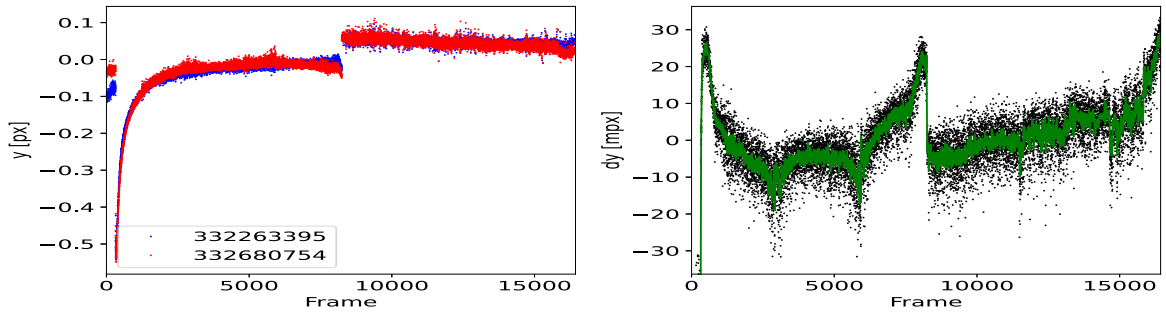

Figure 3. COG estimates on *Y*-axis (left) and difference (right) for target pair {TIC 332263395, TIC 332680754}. Mean values are subtracted, and the filtered data (green line) are superposed to the COG difference.

the observation cover one sector period, corresponding to two orbits, the two larger events (frame no. ∼1000 and ∼8000), separated by about half of the data size, seem to be correlated to the satellite orbit. However, reverse-engineering of TESS is well beyond the scope of our study, and the source of disturbances on the data is not further investigated.

In order to suppress such effects, the long term trend is estimated on the data using a low-pass filter for subsequent removal to evidence the actual dispersion of experimental points. Different filters may be chosen (e.g., Butterworth, Chebyshev, Bessel), resulting in small differences among the residuals with proper parameter choice. In other applications Yusuf et al. (2020), the Savitzky–Golay filter appeared to provide better performance results with respect to the Butterworth filter in terms of noise separation, artifacts and baseline drifts. However, we expect that different filter optimizations could be required for different TESS observations, potentially affected by different disturbances. Our guidelines consist in using an algorithm requiring few parameters, to reduce the amount of information subtracted from the data, and an intermediate window size, which represents a trade-off between prompt response to sudden jumps and good estimate of the underlying trend. In the end, the actual choice (mostly random) is of a Savitzky–Golay filter, with order 3 and window size 31 (green line in the right panel of Figure 2), which appeared to perform reasonably well over our whole sample. The residuals, i.e., the photocenter separation subtracted of the filtered data, have standard deviation 0.47 mpx, corresponding to $1/2127$ pixel.

The *Y* component of the COG is evaluated following the same approach. The Y COG estimate (left) and the *Y* component of source separation (right) for the light curve files of the above target pair ({332263395, 332680754}) is shown in Figure 3. It may be noted that the data dispersion around the filtered data (green line) is affected by a significantly larger noise than the *X* component, resulting in a standard deviation of 4.26 mpx, corresponding to $1/235$ pixel.

The residuals of star separation after suppression of the underlying trend, as estimated by the filtered data, are shown in Figure 4, respectively for *X* (blue) and *Y* (red) components, with an offset of 5 mpx (*X*) and −5 mpx (*Y*) to reduce the overlapping. It may be noted that the noise is not uniform over the time interval; further improvements might be achieved just by selection of lower noise periods, in an approach similar to lucky imaging.

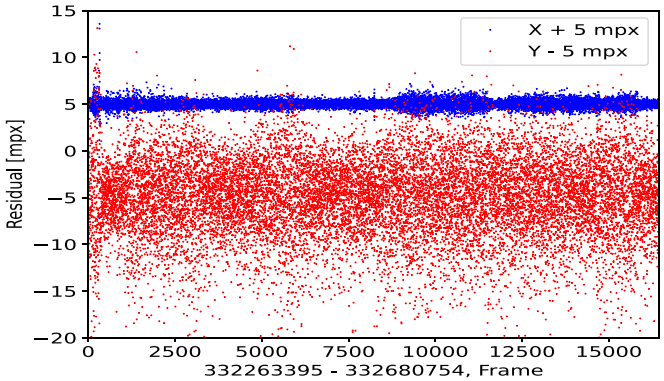

Figure 4. COG residuals on *X* (blue) and *Y* (red) axis for target pair {TIC 332263395, TIC 332680754}, after filtered data subtraction. An offset of 5 mpx (*X*) and −5 mpx (*Y*) is applied for graphical separation.

The histogram of the residual source separation values is shown in Figure 5, respectively on *X* (left) and *Y* (right) coordinates. A Gaussian distribution with matching mean and width is superposed (dotted line) to give a visual impression of the data consistency with white noise only expectations.

3. Results on other Source Pairs

Similar analysis is performed on the other source pairs, whose components are listed in Table 1, in order to verify the generality of the results.

Histograms of the X COG difference residuals are shown in Figure 6 for source pairs {260366549, 297820335} (left) and {393799555, 393800464} (right). The former case includes simultaneous observations of two stars by different CCDs in the same camera, whereas the latter exploits common exposures from a single device. The statistics of star separation

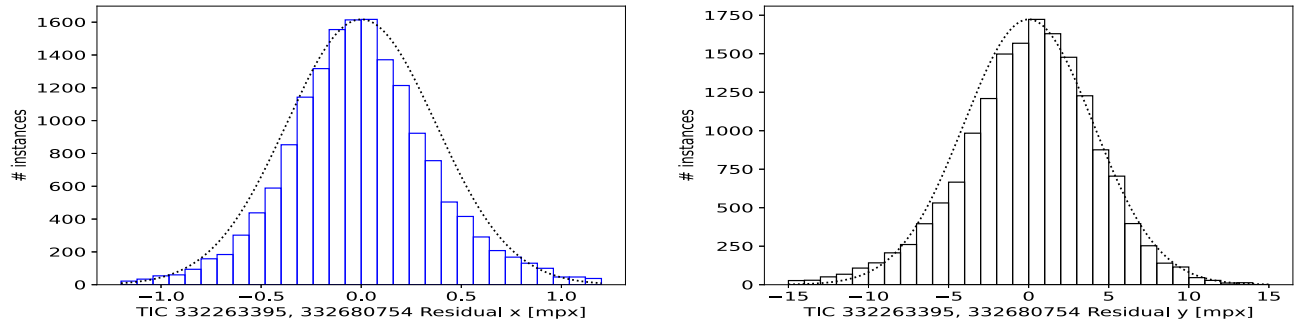

Figure 5. Histogram of residual COG difference around the filtered data, along *X* (left) and *Y* (right) axes, for target pair {TIC 332263395, TIC 332680754}. Dotted line: a Gaussian matching data mean and rms width.

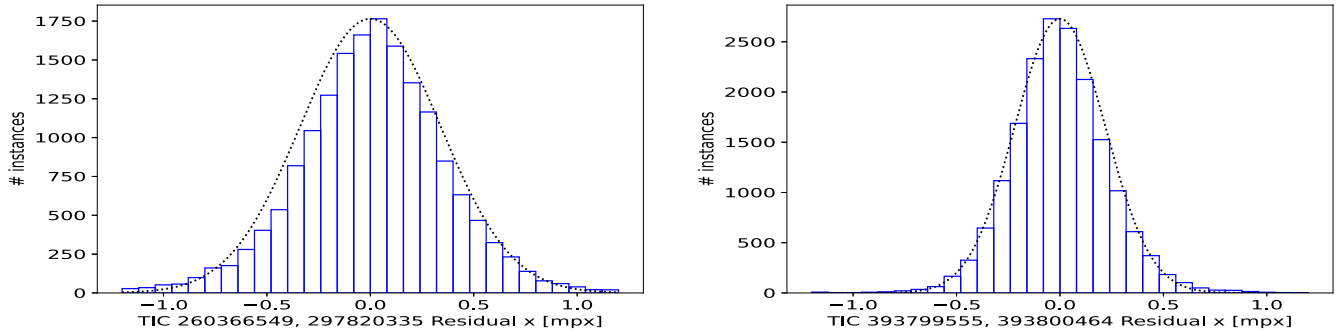

Figure 6. Histogram of residual COG difference, along *X*-axis, for target pairs {TIC 260366549, TIC 297820335} (left), and {TIC 393799555, TIC 393800464} (right). Dotted line: a Gaussian matching data mean and rms width.

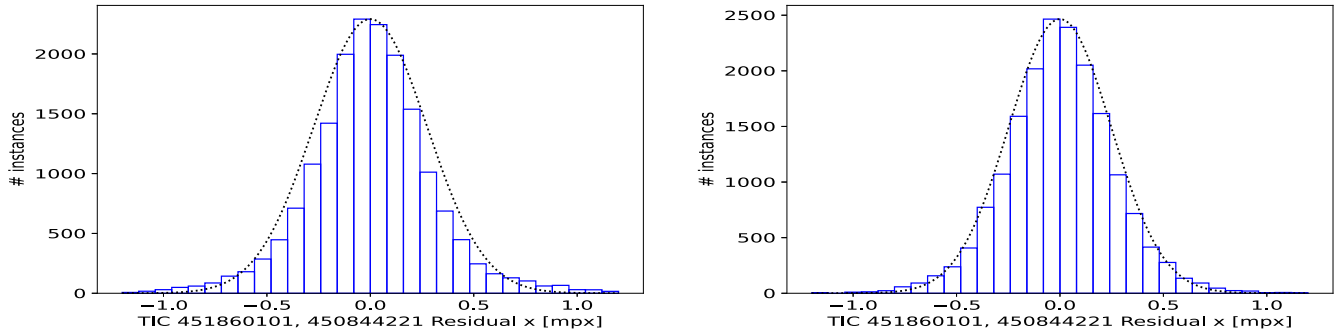

Figure 7. Histogram of residual COG difference, along *X*-axis, for target pair {TIC 451860101, TIC 450844221}, in two observations.

is similar in both cases, thus suggesting that the astrometric stability between focal plane chips is not significantly degraded with respect to that of a single CCD. Therefore, the TESS focal plane appears to have comparable inter-CCD and intra-CCD stability.

In Figure 7, the histogram of separation between targets 451860101 and 450844221 is reported, respectively for two subsequent observations (two epochs). Both observations are affected by pointing errors and instrumental parameter variations of comparable magnitude, but independent. Nonetheless, their residual distributions are quite comparable, evidencing that the astrometric precision remains rather stable.

Plots and histograms similar to the above are available for the other target pairs processed, but they are not included here for brevity. The main statistical parameters of each data set are reported in Tables 2 (*X*) 3 (*Y*). For each target pair, we list the

Table 2
Target COG difference on *X*-axis, Full Data Set (dx) and without Outliers (dx_O)

Target Pair	Frames	Mean dx (px)	Rms dx (mpx)	dx Fraction (1 px^{-1})	Rms dx_O (mpx)	dx_O Fraction (1 px^{-1})
332263395, 332680754	16,435	77.957	0.470	2127.433	0.373	2680.458
94196291, 30906332	17,343	75.312	0.307	3260.464	0.290	3447.213
282326777, 421217840	19,337	89.197	0.173	**5772.257**	0.168	**5963.927**
451860101, 450844221 (1)	17,599	372.739	0.300	3332.148	0.275	3639.047
451860101, 450844221 (2)	17,795	356.833	0.261	3831.469	0.248	4036.312
60986648, 306342251	15,399	296.872	1.729	578.439	1.563	639.860
393799555, 393800464	17,882	59.513	0.240	4167.925	0.219	4564.231
260366549, 297820335	17,059	1800.416	0.374	2674.605	0.341	2936.062

Note. Units: Pixel (px), Milli-pixel (mpx). Best values in bold.

Table 3
Target COG difference on *Y*-axis, Full Data Set (dy) and without Outliers (dy_O)

Target Pair	Frames	Mean dy (px)	Rms dy (mpx)	dy Fraction (1 px^{-1})	Rms dy_O (mpx)	dy_O Fraction (1 px^{-1})
332263395, 332680754	16,435	33.928	4.257	234.881	4.045	247.229
94196291, 30906332	17,343	623.120	1.941	515.205	1.492	**670.381**
282326777, 421217840	19,337	131.213	3.632	275.342	3.023	330.768
451860101, 450844221 (1)	17,599	4.917	1.857	538.632	1.727	578.920
451860101, 450844221 (2)	17,795	132.547	4.310	232.017	4.010	249.353
60986648, 306342251	15,399	279.759	4.344	230.177	1.519	658.267
393799555, 393800464	17,882	55.943	1.818	**550.123**	1.519	658.390
260366549, 297820335	17,059	15.271	4.398	227.367	3.970	251.894

Note. Units: Pixel (px), Milli-pixel (mpx). Best values in bold.

number of good instances (NaN removed), the mean frame coordinate, the rms dispersion and the corresponding pixel fraction, respectively for the whole data set and without the outliers (subscript O, threshold 3σ). The best results (lower uncertainty, higher pixel scaling factor) are evidenced in bold.

The standard deviation of residuals is generally a few 10^{-4} pixels, apart for the source pair {60986648, 306342251}, significantly more degraded (1.7 mpx), as justified by the fainter magnitude ($G \sim 7$ mag) of the former component. The Y COG difference residuals are generally more noisy, by about one order of magnitude (a few 10^{-3} pixels). This aspect will be discussed in more detail in Section 4.1.

4. Discussion

The results of our analysis are in agreement with the expectation of very low uncertainty on image location in case of very high S/N, as represented in Equation (1), and verified by the detected separation between bright stars. However, a few aspects are worth commenting, either to gain some understanding on the underlying detector physics (Section 4.1), or to derive potential elements of interest for future high precision astrometry missions (Sections 4.2, 4.3).

4.1. Detector Effects

The precision achieved along (Y) and across (X) the CCD columns is quite different, with values significantly more appealing in the latter case (Tables 2 and 3). The issue can be clarified by a more in-depth look into the data properties.

A few examples are shown in Figure 8, for the selected observation of targets 306342251, 282326777, 297820335, 450844221 and 332263395 (top to bottom). The X-axis in figure is oriented along the CCD columns. The selected targets are very bright; their detected signal level, listed in Table 4, scales according to magnitude and spectral type. Comparing the five cases, it may be noted that the image size along Y (across CCD columns) is similar, whereas it increases progressively, top to bottom, along the X-axis, according to the rms image width also listed in Table 4. The other sources in our sample evidence comparable behavior, i.e., along column width increasing with the signal level detected by TESS according to source spectrum and instrument electro-optical response (the Gaia magnitude is not a unique indication here).

We remind that, for faint to intermediate magnitudes, the detected signal is distributed according to the shape of the optical PSF, but this behavior changes when the pixel potential well is filled. The photoelectrons of bright stars, generated in

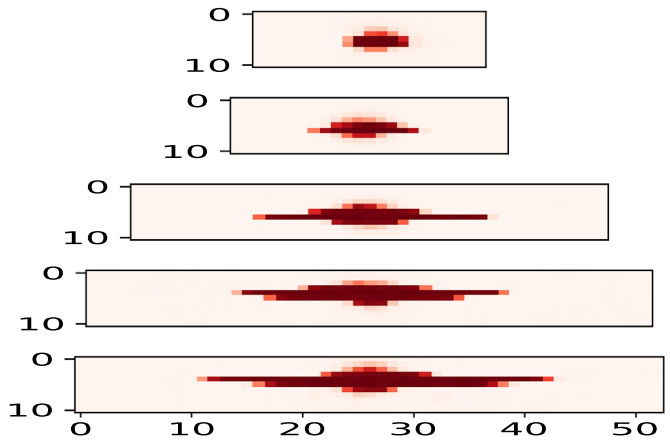

Figure 8. Median frame for targets TIC 306342251, TIC 282326777, TIC 297820335, TIC 450844221 and TIC 332263395 (top to bottom). The increasing horizontal size of the images is due to saturation.

Table 4
Target Signal Level of Moderately Saturated Stars

Target TIC	Flux (e^- s^{-1})	Rms Width (px)
306342251	1.763e6	1.536
282326777	2.237e6	2.283
297820335	4.793e6	4.534
450844221	6.711e6	5.703
332263395	7.024e6	7.033

the pixels associated to the peak of the PSF, may easily spill along the columns to neighboring pixels, in the phenomenon commonly called "bleeding." The physical reason is that the accumulated charge compensates the local potential well, generating an electrical field with opposite sign, so that new charges generated by the photoelectric effects no longer "feel" a local constraint, and propagate further on. The column separation, achieved by masking and doping rather than an electric potential applied to the electrodes, is much more "robust."

Therefore, the detected signal no longer matches the optical PSF, acquiring larger and larger size in the direction of the CCD columns. The images of saturated stars are thus significantly larger than the diffraction size $\sim\lambda/D$. As a consequence, in spite of the increasing photometric S/N, the location uncertainty no longer improve significantly, rather evidencing a sort of graceful degradation.

In practice, Equation (1) might be modified for partially to moderately saturated images, e.g., by replacing the geometric term corresponding to the diffraction limit λ/D with the current effective width. Such effective width, along CCD columns, can be expected to increase more or less linearly with the photon count N, also according to Table 4, whereas the S/N grows as $\sqrt{N}$; consequently, that component of the astrometric uncertainty on very bright stars may be expected to increase approximately as $\sqrt{N}$.

Also, the estimate of the distance between sources is affected by the cumulative noise from both of them, which in the non-saturated regime is dominated by the fainter one. Conversely, in the moderately saturated regime, the limiting factor may be imposed by the brighter source. At the same time, the astrometric uncertainty component across CCD columns can be expected to keep on improving as $\sim 1/\sqrt{N}$.

This framework seems to justify qualitatively the different performance achieved along the two axes, as reported in Tables 2 and 3.

Detector saturation still allows for high precision measurement, at least in one direction. This effect is not fully exploited by Gaia, since the design approach privileged preservation of the image quality also for bright targets, adopting on-chip anti-bleeding circuitry, and SW controlled gates actually reducing the exposure time of bright objects.

4.2. Calibration of the Instrument Electro-optical Response

Recalling the long term drifts and sudden jumps in the data evidenced by Figures 2 and 3, they were ascribed in Section 2.2 either to variations in the electro-optical parameters of the instrument, or to calibration artefacts which might mimic such effects. It is conceivable that further insight on TESS behavior might be achieved by detailed investigation of the field and time dependence of these effects for any CCD and camera; this may even lead to (conceivably minor) improvements on calibration of science data. However, such investigation on potential origin of the effects is basically impossible without a complex effort of payload reverse-engineering, based on the full set of technical data of the mission. A phenomenological approach quantifying data correlations is simpler and, potentially, nearly as effective.

The issue of instrument calibration is of course of paramount relevance to future astrometric missions, but it is well beyond the scope of this study, mostly focused on demonstration of the achievable precision, rather than accuracy. The filtered data subtraction on COG difference, adopted to factor out apparent systematic behaviors, can be considered one such phenomenological approach.

A hardware approach at control of the systematic errors can be applied by design, minimizing the instrument optical response variation Riva et al. (2020), and/or including a metrology subsystem able to keep track of the variation and allow for its correction. Remarkable experimental results have been achieved e.g., on interferometric calibration of a detector Crouzier et al. (2016), to the order of a few 10^{-5} in static conditions.

Notably, Gaia uses both on-board metrology, the Basic Angle Monitoring (BAM) device (Gielesen et al. 2012; Gai

Table 5
Collective Uncertainty on Target Separation, on X (σ_{xC}) and Y (σ_{yC}) Axes

Target Pair	σ_{xC} (μpx)	σ_{yC} (μpx)
332263395, 332680754	2.329	14.739
94196291, 30906332	3.667	33.210
282326777, 421217840	**1.246**	26.118
451860101, 450844221 (1)	2.262	13.995
451860101, 450844221 (2)	1.957	32.310
60986648, 306342251	13.931	35.010
393799555, 393800464	1.794	**13.594**
260366549, 297820335	2.863	33.674

Note. Units: micro-pixels (μpx). Best values in bold.

et al. 2015), and calibration based on science data. The Gaia approach to calibration are described in detail in the literature (Abbas et al. 2017; Lindegren et al. 2021).

Besides, the inter-CCD stability result from Section 3 suggests that the TESS focal plane technology appears to be compatible with some of the stability requirements of future astrometry missions.

4.3. Cumulative Performance

The observing sequences used in our analysis can in principle be piled up to provide the result corresponding to a single exposure integrating over the whole period. This is not conceptually different from the digital stacking of 2 s frames already implemented in TESS and building up its 120 s elementary exposures, as recalled in Section 2.

Apart the issue of systematic error suppression discussed in Section 4.2, the sampling distribution of star separation residuals (Figures 5–7) is, in all cases taken into account, a bell-shaped curve reasonably similar to a Gaussian with characteristic width σ corresponding to the data rms dispersion. The uncertainty on the center of the distribution of N elementary measurements is, from basic statistics, of the order of $\sigma/\sqrt{N}$.

Applying such considerations to the results of our analysis (Tables 2 and 3), using the rms from the fourth column as σ (thus including outliers), and the number of good samples from the second column as N, we get the uncertainty on the *collective* estimate of source separation on either axis, namely σ_{xC} and σ_{yC}. The values are listed in Table 5, reported in (impressive, in our opinion) micro-pixel (μpx) units.

The precision achieved across CCD column (X) is, in the best case (in bold), slightly above 1 μpx, and it is in several cases within a few μpx. In the along CCD column direction (Y), the performance is about one order of magnitude worse, i.e., a few 10 μpx. Since TESS pixels have angular size 21″, this nominally results in an on-sky precision ranging between a few 10 μas and a few 100 μas.

Similar considerations may be applied to the case of a future 1 m class telescope, endowed with ∼50 mas pixels, in which the 1 μpx precision level would correspond to ∼0.05 μas, consistently with the goals and photon limited performance of e.g., Theia (Malbet et al. 2021) and RAFTER (Riva et al. 2020).

It may be noted that the performance difference in the two coordinates appears to be mainly due to CCD saturation and bleeding. The situation might be improved by a more flexible readout scheme, to be applied in the bright star regime, in which the elementary exposure time is shorter than 2 s, to prevent saturation, and digital co-adding is exploited to pile up data to the desired full integration. The precision on both coordinates of bright stars may thus be expected to be preserved, at least on a larger magnitude range than that provided by a naive fixed-duration exposure strategy.

The cost of this approach consists in more stringent requirements on the on-board data processing power (I/O, CPU, memory, telemetry), and some performance degradation on intermediate to faint brightness stars close to bright sources. Suitable trade-offs may be devised in the definition studies of future missions.

The most immediate candidate for the application of such optimization techniques is obviously the PLATO[4] (Planetary Transits and Oscillations of Stars) mission (Rauer & Heras 2018), the M3 ESA mission in the Cosmic Vision 2015–2025 Plan, which inherits from TESS the approach of exoplanet detection with the transit technique, but aims at characterization of Earth-sized planets in the habitable zone of Sun-like stars, rather than detection of rocky planets around M-dwarfs. The potential benefit consists in better solution of complex exoplanetary systems, e.g., including multiple bodies, by simultaneous exploitation of photometric and astrometric variation.

Future high precision astrometry missions, e.g., Theia and TOLIMAN, will also benefit of such approach: flexible elementary exposure time, accumulation of large sets of elementary exposures building up longer integration, exploitation of saturated images of very bright targets appear to be convenient building blocks for the design of reliable measurements in the challenging 10^{-6} pixel realm.

5. Conclusions

We investigate the geometric limiting precision on stellar image location, in terms of CCD pixel fraction, by analysis of the statistics of star pair separation on selected sets of images, from the publicly available science data of the TESS mission. The star coordinates computed by the TESS pipeline appear to be affected by jumps, long term variation and noisy periods, at the few 0.1 pixel level; the coordinate difference, i.e., star separation, reduces such noise by one order of magnitude, to ∼0.01 pixel, factoring out common mode pointing errors, but it is still affected by large time dependent variations. After

[4] https://platomission.com/

removal of such trends by simple filtering techniques, the residuals, which we consider representative of the limiting astrometric noise, have rms dispersion at the level of a few milli-pixels, along the CCD columns, or below 1 mpx in the across column direction, down to better than 1/5000 pixel.

Our interpretation of such findings is based on CCD saturation, increasing the detected image size in a preferential direction, and degrading at the same time that component of the location uncertainty. The astrometric precision is mostly preserved across the CCD columns, where the image size remains close to the diffraction limit.

Cumulative performance of large sets of images, assuming appropriate removal of the systematic trends, corresponds to uncertainties of order of a few micropixels across CCD columns, and a few ten micropixels along columns. Such results appear to be encouraging with respect to feasibility of nearly photon limited precision in future high precision astrometry missions.

The activity has been partially funded by the grant Astrometric Science and Technology Roadmap for Astrophysics (ASTRA) from the Italian Ministry of Foreign Affairs and International Cooperation (MAECI), and by the Italian Space Agency (ASI) under contract 2018-24-HH.0. This study made use of Lightkurve, a Python package for Kepler and TESS data analysis (Lightkurve Collaboration et al. 2018). The TESS data used in this study can be obtained from MAST in reduced and calibrated format (https://mast.stsci.edu/). Auxiliary data on targets from SIMBAD (CDS).

ORCID iDs

M. Gai https://orcid.org/0000-0001-9008-134X
A. Vecchiato https://orcid.org/0000-0003-1399-5556
M. Lattanzi https://orcid.org/0000-0003-0429-7748

References

Abbas, U., Bucciarelli, B., Lattanzi, M. G., et al. 2017, PASP, 129, 054503
Astropy Collaboration, Price-Whelan, A. M., Sipőcz, B. M., et al. 2018, AJ, 156, 123
Astropy Collaboration, Robitaille, T. P., Tollerud, E. P., et al. 2013, A&A, 558, A33
Bendek, E., Mamajek, E., Vasisht, G., et al. 2021, AAS Meeting Abstracts, 53, 318.02
Borucki, W. J., Koch, D.Kepler Science Team, et al. 2010, AAS/DPS Meeting Abstracts, 42, 47.03
Crouzier, A., Malbet, F., Henault, F., et al. 2016, A&A, 595, A108
Gai, M., Busonero, D., & Cancelliere, R. 2017, PASP, 129, 054502
Gai, M., Carollo, D., Delbò, M., et al. 2001, A&A, 367, 362
Gai, M., Casertano, S., Carollo, D., & Lattanzi, M. G. 1998, PASP, 110, 848
Gai, M., Qi, Z., Lattanzi, M., et al. 2020a, Proc. SPIE, 11451, 114514I
Gai, M., Vecchiato, A., Busonero, D., et al. 2015, Metrology for Aerospace (MetroAeroSpace), 329
Gai, M., Vecchiato, A., Riva, A., et al. 2020b, Proc. SPIE, 11443, 114430N
Gaia Collaboration, Brown, A. G. A., Vallenari, A., et al. 2020, A&A, 649, A1
Gielesen, W., de Bruijn, D., van den Dool, T., et al. 2012, Proc. SPIE, 8442, 84421R
Gil Otero, R., Mackie, R., Greenaway, C., et al. 2021, Proc. SPIE, 11852, 118520S
Guerrero, N., Seager, S., Huang, C., et al. 2021, ApJS, 254, 39
Harris, C. R., Millman, K. J., van der Walt, S. J., et al. 2020, Natur, 585, 357
Howell, S. B., Sobeck, C., Haas, M., et al. 2014, PASP, 126, 398
Hunter, J. D. 2007, CSE, 9, 90
Lightkurve Collaboration, Cardoso, J. V. d. M., Hedges, C., et al. 2018, Lightkurve: Kepler and TESS Time Series Analysis in Python, Astrophysics Source Code Library, ascl:1812.013
Lindegren, L. 1978, in IAU Coll. 48: Modern Astrometry, ed. F. V. Prochazka & R. H. Tucker, 197
Lindegren, L., Klioner, S. A., Hernández, J., et al. 2021, A&A, 649, A2
Malbet, F., Boehm, C., Krone-Martins, A., et al. 2021, ExA, 51, 845
Mendez, R. A., Silva, J. F., Orostica, R., & Lobos, R. 2014, PASP, 126, 798
Prusti, T., De Bruijne, J., Brown, A., et al. 2016, A&A, 595, A1
Rauer, H., & Heras, A. M. 2018, Space Missions for Exoplanet Science: PLATO (Berlin: Springer)
Ricker, G., Winn, J., Vanderspek, R., et al. 2015, JATIS, 1, 014003
Riva, A., Gai, M., Vecchiato, A., et al. 2020, Proc. SPIE, 11443, 114430P
Stassun, K. G., Oelkers, R. J., Paegert, M., et al. 2019, AJ, 158, 138
Stassun, K. G., Oelkers, R. J., Pepper, J., et al. 2018, AJ, 156, 102
Tuthill, P., Bendek, E., Guyon, O., et al. 2018, Proc. SPIE, 10701, 107011J
Yusuf, S. D., Maduakolam, F. C., Umar, I., et al. 2020, Asian J. Res. Cardiovascular Diseases, 2, 15